Research Paper

Sensitive *in vivo* Visualization of Breast Cancer Using Ratiometric Protease-activatable Fluorescent Imaging Agent, AVB-620

Marcel Miampamba[1]*, Junjie Liu[1]*, Alec Harootunian[1], Andrew J Gale[1], Stephen Baird[2], Steven L Chen[1], Quyen T Nguyen[2], Roger Y Tsien[3, 4, #] and Jesús E González[1]✉

1. Avelas Biosciences, 11099 N. Torrey Pines Road, Suite 290, La Jolla, CA, USA;
2. School of Medicine, University of California, San Diego, La Jolla, CA, USA;
3. Department of Chemistry & Biochemistry, University of California, San Diego, La Jolla, CA, USA;
4. Howard Hughes Medical Institute.

* Contributed equally to this work.

Deceased.

✉ Corresponding author: tgonzalez@avelasbio.com, Avelas Biosciences, 11099 N. Torrey Pines Road, Suite 290, La Jolla, CA 92037

Abstract

With the goal of improving intraoperative cancer visualization, we have developed AVB-620, a novel intravenously administered, *in vivo* fluorescent peptide dye conjugate that highlights malignant tissue and is optimized for human use. Matrix metalloproteinases (MMPs) hydrolyze AVB-620 triggering tissue retention and a ratiometric fluorescence color change which is visualized using camera systems capable of imaging fluorescence and white light simultaneously. AVB-620 imaging visualizes primary tumors and demonstrated high *in vivo* diagnostic sensitivity and specificity (both >95%) for identifying breast cancer metastases to lymph nodes in two immunocompetent syngeneic mouse models. It is well tolerated and single-dose toxicology studies in rats determined a no-observed-adverse-effect-level (NOAEL) at >110-fold above the imaging and estimated human dose. Protease specificity and hydrolysis kinetics were characterized and compared using recombinant MMPs. To understand the human translation potential, an *in vitro* diagnostic study was conducted to evaluate the ability of AVB-620 to differentiate human breast cancer tumor from healthy adjacent tissue. Patient tumor tissue and healthy adjacent breast tissue were homogenized, incubated with AVB-620, and fluorogenic responses were compared. Tumor tissue had 2-3 fold faster hydrolysis than matched healthy breast tissue; generating an assay sensitivity of 96% and specificity of 88%. AVB-620 has excellent sensitivity and specificity for identifying breast cancer in mouse and human tissue. Significant changes were made in the design of AVB-620 relative to previous ratiometric protease-activated agents. AVB-620 has pharmaceutical properties, fluorescence ratio dynamic range, usable diagnostic time window, a scalable synthesis, and a safety profile that have enabled it to advance into clinical evaluation in breast cancer patients.

Key words: Breast cancer, imaging, fluorescence-guided surgery, activatable cell penetrating peptide, matrix metalloproteinase.

Introduction

Intraoperative visualization of malignant tissue is particularly important in breast cancer. The predominant operation performed is a lumpectomy which strives to remove only the portion of the breast with cancer while achieving a negative margin, currently defined as no tumor on the edge of the removed specimen. Failure to achieve negative margins is associated with an increase in breast cancer recurrence and thus generally necessitates a second operation to remove more breast tissue, or sometimes the remainder of the breast (1). In addition, identification of malignant lymph nodes is considered

to be one of the most prognostic factors, along with tumor size and known metastatic spread, in determining long term survival (2). Thus, rapid and accurate identification of disease spread is important to determine the extent of surgical as well as adjuvant treatments.

One promising approach to provide surgeons intraoperative cancer localization is to employ *in vivo* fluorescent cancer imaging agents in combination with imaging camera systems, or fluorescence image-guided surgery (FIGS) (3–5). Fluorescence imaging is compatible with real-time surgical application requirements with high sensitivity, spatial and temporal properties, unlike PET and MRI which require longer acquisition times and have reduced spatial resolution. However, like other light-based methods, fluorescence has limited tissue penetration which restricts visualization to tissues near surface. Thus, FIGS is well matched with current optical visualization methodology in regard to view but offers complementary molecular information which can improve cancer visualization accuracy.

To enable FIGS requires design, generation and development of *in vivo* fluorescent agents that provide sufficient signal, contrast, and specificity in cancer patients. To achieve this goal, various molecular approaches are being explored and evaluated. Early cancer FIGS focused on 5-ALA and prodrug versions that enhance porphyrin biosynthesis and associated fluorescence in cancer tissue (6). A variety of more recent approaches have been described that include fluorescently labeled: antibodies (7–10), small-molecule receptor ligands (11), peptides (12), lipids (13), and protease-activated agents (10, 14–21). Several investigational agents have entered clinical evaluation (15, 22–24).

The ideal agent would be systemically administered in a saline formulation for unbiased and broad tissue applicability, potent, easy to manufacture, safe, fast acting, bright, have high diagnostic sensitivity and specificity, generate a stable signal compatible with surgery schedules and operating room environment, and applicable to a large percentage of cancer patients. Building on the pioneering work of Weissleder lab on protease dependent fluorescence agents (19,25) and the Tsien lab on activatable cell penetrating peptides (ACPP) (14), we have designed and developed a intravenously (IV) administered fluorescent peptide dye conjugate that achieves these performance criteria. It utilizes the increased proteolytic activity, including that from matrix metalloproteinases (MMPs) in tumors and the surrounding stromal microenvironment, known to be important for cancer progression, invasion, and metastasis (26). MMP2 and MMP9 have higher proteolytic activity in human breast carcinoma and surrounding stromal microenvironment tissue (27, 28) and MMP14 has been linked to many cancers (29–33).

In addition to significant cancer specificity challenges, factors such as agent biodistribution and concentration, tissue shape, motion in the surgical field, illumination distance and homogeneity affect the detected fluorescence intensity. As a result, determining an absolute fluorescence intensity threshold for a potential diagnostic agent is very challenging. To attenuate these confounding factors we have further engineered a ratiometric fluorescence readout that results from efficient FRET between Cy5 and Cy7 fluorophrores in intact AVB-620. Protease-mediated hydrolysis disrupts energy transfer and causes a large Cy5/Cy7 fluorescence ratio (FR) change (increase in Cy5 and decrease in Cy7). The FRET mechanism coupled with ratio imaging enables a robust readout that is much less prone to optical artifacts that limit single intensity fluorescent probe readouts. The advantages of *in vivo* fluorescence ratio imaging have been described (34). Here we report the design, synthesis, enzyme kinetics, *in vivo* and *ex vivo* breast cancer detection activity, and safety of AVB-620. The combination of improved pharmaceutical properties, FR detection, dynamic range, *in vivo* diagnostic performance, kinetics, and safety provides a superior preclinical profile compared to previously described ratiometric ACPPs (34). These improvements enable and provide compelling rationale for advancement to clinical evaluation.

Materials and Methods

Materials

HPLC-grade acetonitrile was purchased from Fisher Scientific (Philipsburg, PA). Purified water was obtained using a Milli-Q water purification system (Millipore, Bedford, MA). Trifluoroacetic acid (TFA), Dimethylformamide (DMF) and *N*-methylmorpholine (NMM) were purchased from Sigma-Aldrich (Milwaukee, WI). α-aminoxyl-ω-methoxy, polyoxyethylene (Mw~2,000) [mPEG(2K)-ONH$_2$] was from NOF America Corporation (Irvine, CA) and the peptide core from PolyPeptide Group (San Diego, CA).

Recombinant protease materials were used. Human MMP2, human MMP9, human MMP1, human MMP3 and human MT1-MMP (MMP14), and mouse MMP2 and mouse MMP9 were purchased from R&D Systems (Minneapolis, MN). Human MMP7 and MMP8, active human MMP13 and the catalytic domains of MT2-MMP (MMP15) and

MT4-MMP (MMP17) were purchased from EMD Millipore (Billerica, MA). The catalytic domain of MMP11 was purchased from Enzo Life Sciences (Farmingdale, NY). The catalytic domain of MMP19 was purchased from Sino Biological (Beijing, China). Where necessary, pro-enzymes were activated according to the manufacturer's instructions. The MMP inhibitors GM6001 (Ilomastat) and Prinomastat were purchased from EMD Millipore and Sigma Aldrich (St. Louis, MO) respectively.

Human Tumor Samples

Matched human breast cancer and normal tissue samples were obtained through the Cooperative Human Tissue Network (CHTN). Collection and use of these samples were approved by the CHTN Institutional Review Board.

Analytical and HPLC Methods

LC-MS analysis was carried out on a computerized Waters 2695 separation module equipped with a Waters 2487 dual λ absorbance detector combined with the Finnigan LCQ Deca XP mass spectrometer, Peeke Scientific column (Titan 200 5µm, C18-MC, 50 × 2.1 mm), and Xcalibur analytical software (Thermo Fisher Scientific, Waltham, MA).

HPLC purification was carried out on a Waters PrepLC System equipped with a Waters 2487 dual λ absorbance detector, Fraction Collector III, Phenomenex column (Kinetex, 5µ, C18, 100Å AXIA 150 × 30 mm) and Masslynx analytical software (Waters, Milford, MA). The mobile phase consisted of a water (0.05% TFA) (solvent A)/acetonitrile (0.05% TFA)(solvent B) gradient.

AVB-620 synthesis (see scheme, Fig. S1)

To a solution of peptide **1** (200 mg, 49.6 µmol) in DMF (5 mL) at room temperature and protected from light, Cy5 maleimide (60 mg, 65.6 µmol) and *N*-methylmorpholine (80 µL, 0.73 mmol) were added and mixed with stirring. The reaction was followed by LC-MS and completed in 1 h. Ether (40 mL) was added to the mixture and the precipitate collected after centrifuge, washed with ether (40 mL × 2) and purified by HPLC to afford the intermediate **2** (141 mg, 61%). Calculated: $[M+3H]^{3+}$ ($C_{152}H_{242}N_{51}O_{43}S_4$) m/z = 1200; Found ESI: $[M+3H]^{3+}$ ($C_{152}H_{242}N_{51}O_{43}S_4$) m/z = 1200.

To a solution of intermediate **2** (101 mg, 21.8 µmol) in DMF (10 mL) at room temperature were added Cy7 carboxylic acid, succinimidyl ester (40 mg, 41.1 µmol) and *N*-methylmorpholine (0.2 mL, 1.8 mmol). The resulting mixture was stirred in dark at room temperature for 36 h before adding 35 mL of Ether. The precipitate was collected after centrifugation and washed with ether (40 mL × 2). Purification of the mixture by RP-HPLC afforded intermediate **3** (28.1 mg, 25%) and the recovery of **2** (63 mg). Calculated: $[M+3H]^{3+}$ ($C_{187}H_{282}N_{53}O_{50}S_6$) m/z = 1421; Found ESI: $[M+3H]^{3+}$ ($C_{187}H_{282}N_{53}O_{50}S_6$) m/z = 1421.

The mixture of intermediate **3** (28.1 mg, 5.4 µmol) and mPEG(2K)-ONH$_2$ (17 mg, 7.6 µmol) in glycine buffer (4 mL, 0.1 M, 20 mM aniline, pH 3.0) and acetonitrile (0.8 mL) was stirred in dark at room temperature for 24 h. After the reaction was complete, acetophenone (10 µL, 86 µmol) was added to the solution. The mixture was stirred at room temperature for 2 h. Purification by RP-HPLC afforded pure (99.1%) AVB-620 (25.0 mg, 63%). Purity was assessed by analytical HPLC (Fig. S1B) and identity was confirmed by MALDI-TOF MS using a THAP matrix (Fig. S1C). The MS showed expected mass envelope of AVB-620 around 6500 amu and PEG ladder peaks (+/- 44 amu) from conjugated polydisperse PEG moiety.

Fluorescence spectroscopy

Fluorescence spectroscopy was performed on a Fluorolog spectrometer (Horiba Instruments, Irvine, CA). Lyophilized AVB-620 (Lot # GI0909) was solubilized in 50 mM Tris, pH 7.5, 10 mM CaCl$_2$, 150 mM NaCl, 0.05% Brij35 (TCNB) buffer shortly before the experiment. For MMP cleavage 10 µM of AVB-620 solution was incubated with 20 nM MMP9 for 2.5 h in the dark at 37°C. The stock solution (± cleavage) was then diluted to 0.4 µM in TCNB buffer and fluorescence spectra were recorded with excitation at 630 nm, 3 nm slit width and emission recorded from 620 to 850 nm, 3 nm slit width. Fluorescent intensity was corrected for variability in amperage of the lamp and the wavelength-specific intensity of the lamp.

Kinetics of AVB-620 cleavage by MMPs

Activity assays were performed in TCNB buffer. Where possible active concentration of purchased MMPs was determined independently by active site titration with the MMP inhibitors GM6001 (MMP1, MMP2, MMP9,) or Prinomastat (MMP3, MMP13, MMP14). The enzyme was pre-incubated at a putative concentration of 25 nM with inhibitor concentrations ranging from 5-50 nM (8 concentrations) then remaining activity was measured by cleavage of AVB-620 on a fluorescence plate reader as described below.

For kinetic determination of enzymatic activity, concentrations of MMPs were fixed at 1-20 nM depending on which enzyme was being tested. AVB-620 was titrated in a 2-fold dilution series most commonly from 0.16 µM to 5 µM. MMP2 and MMP9

had AVB-620 titrations up to 10 µM. Each condition was assayed in triplicate in 384 well black polypropylene plates (Costar, Corning Inc., NY). Wells containing the solutions being assayed were surrounded with a ring of wells containing 50 µL H$_2$O each and all were covered with a clear adhesive sealing film (Cat. # 08-408-240, Fisher Scientific, Pittsburgh, PA) in order to prevent evaporation. Reactions were initiated by addition of enzyme and fluorescence was measured using a Molecular Devices (Sunnyvale, CA) fluorescence plate reader (SpectraMax M2 or FlexStation 3). Excitation and emission were 620 and 670 nm respectively with a cut off filter at 630 nm. 100% cleaved AVB-620 controls were included in each assay to convert relative fluorescence units to molar concentration of cleaved AVB-620, and uncleaved AVB-620 blanks were subtracted out. Kinetic constants were determined at 37 °C (except for MMP17, which was measured at room temperature due to instability at 37 °C). Initial cleavage rates at each concentration were determined from the linear portion of the fluorescence time courses and velocity was graphed relative to concentration of AVB-620. In these experiments, K_m was estimated to be much greater than the highest concentration of AVB-620 used. Therefore, the Michaelis-Menten equation reduces as follows:

$$v = [E]*[S]*k_{cat}/K_m$$

Thus these data graphed as a straight line with a slope of k_{cat}/K_m when [E] is divided out. Because K_m was much larger than the practical substrate concentration, we could determine the specificity constant (k_{cat}/K_m) but could not accurately determine k_{cat} and K_m separately.

Protease activity in tissue homogenates

Mouse or human tumor and control tissues were homogenized as follows: Individual tissue samples were cut into 50-90 mg pieces which were dispensed into 1.5 mL pre-chilled microtubes. The tissue pieces were weighed and 10 µl of TCNB buffer per mg tissue were added to each piece. Each piece was then diced finely with dissecting scissors. Diced tissue samples were then homogenized by sonication with a microtip on wet ice (Total time: 2 min; Pulse: 2 sec ON – 3 sec OFF; Amplitude > 50%; VCX500 Vibracell Sonicator, Sonics & Materials Inc., Newtown, CT). Tubes were then centrifuged at 15,000 x g for 20 minutes at 4°C and the supernatants (homogenates) collected. All supernatants from each individual tissue sample were pooled, then sub-aliquoted and stored at -80 °C.

AVB-620 cleavage was measured for each homogenate in triplicate as follows: Homogenates were thawed and stored on ice. Each homogenate was diluted 1:1 with TCNB buffer then incubated at 37 °C for 1 h. 5 µL of 5 µM AVB-620 was added to each well in a 384 well plate followed by 45 µL of 1:1 homogenate. The plate was sealed with a clear adhesive film and the fluorescence read every 5 minutes for 10 h at room temperature using a Molecular Devices (Sunnyvale, CA) fluorescence plate reader. Fluorescence was read using an excitation of 620 nm and emission of 670 nm for Cy5 signal, excitation of 620 nm and emission of 773 nm for Cy7 FRET signal from Cy5, and excitation of 720 nm and emission of 773 nm for Cy7 signal. Cleavage rates were measured as a change in FR per minute. The FR was the ratio of Cy5 fluorescence (excitation 620 nm, emission 670 nm) over Cy7 FRET fluorescence (excitation 620 nm, emission 773 nm). The rate was determined as the slope of this FR over the first 5 h of the reaction.

MMP2 and MMP9 activities were visualized in the tissue homogenates using Novex gelatin 10 % zymogram gels (Life Technologies, Carlsbad, CA) according to the recommended protocol. 10 µL of homogenate was loaded per lane. Select samples were run in gels with titrations of MMP2 or MMP9 included as standard curves to estimate concentration of MMPs in tumor and normal adjacent tissues. The identified MMP2 band was quantified using ImageJ analysis of digital photographs of the gels. It was not possible to conclusively quantify MMP9 because MMP9 consists of multiple bands, some of which closely overlap with the putative proMMP2 band.

Determination of MMP concentration by ELISA

Tissue homogenates from representative paired samples were sent to Quansys Biosciences (Logan, Utah) where they were analyzed with the Quansys multiplex Q-Plex ELISA for concentration of total MMP1, MMP2, MMP3, MMP7, MMP9, and MMP13. Concentration in homogenate was converted to concentration in tissue by multiplying by the dilution factor created by the above protocol for homogenate generation.

In vivo Models

The mouse ear tumor model of lymphatic and cervical lymph node metastasis used for imaging agent evaluation was developed based on modification of the method described for a melanoma model (35). Metastatic 4T1 tumor cells from ATCC (CRL-2539™) were grown and suspended in DPBS/Matrigel™ (1:1 vol) and then injected subcutaneously (4 x 10^5 tumor cells/50 µL/mouse) in female BALB/c mice on the right ear pinna above the auricular cartilage under ketamine-xylazine

anesthesia. Similarly, polyoma middle T 8119 mammary carcinoma tumor cells (PyMT) obtained from Dr. Lesley Ellies (Department of Pathology, University of California, San Diego, CA 92093) were grown and suspended in DPBS/Matrigel™ (1:1 vol) and injected subcutaneously in female C57BL/6 mice as above. In both cases ear tumor growth was followed by cervical lymph node metastasis by migration of cancer cells to lymph nodes as previously described (35). AVB-620 was tested using ear tumor-bearing mice 17-20 (4T1 tumor model) or 14-24 (PyMT tumor model) days post auricular tumor cell implantation. Tumor-bearing mice were randomly selected, restrained using the rotating tail injector (Braintree Scientific, Inc., MA) and dosed IV (tail vein) with AVB-620 solution (60 µM AVB-620; 100 µL/~20 grams mouse, i.e., 1.8 mg/kg body weight). After dosing, each tumor-bearing mouse was returned to its assigned housing cage and kept under controlled environmental conditions (food and water ad libitum) before being studied. A total of 30 4T1 tumor-bearing mice were examined at 3 h (N=9) and 6 h (N=21) post AVB-620 administration. Twenty-four PyMT tumor-bearing mice were examined 6 h post-AVB-620 administration.

Imaging Procedures and Hardware

Primary tumor and cervical lymph nodes were imaged *in vivo* in ear tumor-bearing mice terminally anesthetized with a mixture of Ketamine HCl/Xylazine HCl (100 mg/kg ketamine - 10 mg/kg xylazine) administered intraperitoneally. Each mouse underwent a blunt dissection of ipsilateral (ear tumor side) and contralateral cervical lymph nodes. Following surgery, six major visible superficial cervical lymph nodes (including both ipsilateral and contralateral nodes) were identified, moisturized with physiological saline (0.9% Sodium Chloride Irrigation USP, B. Braun Medical Inc., Irvine, CA) and imaged using various systems including: SZX10 fluorescence stereomicroscope (Olympus Optical, CO, Ltd, Tokyo, Japan) linked to HCImage software for image acquisition from Hamamatsu (Hamamatsu Photonics, K.K., Systems Division, Shizuoka-Pref, Japan); and a customized Navitar Imaging System (Navitar Inc, Rochester, NY) interfaced with Spot Software 5.0 for image acquisition (SPOT™ Imaging Solutions, Sterling Heights, MI). All the above-mentioned fluorescence imaging systems were equipped with an LED light source ~630 +/- 20 nm to excite Cy5 fluorophore and two emission filters to separately capture Cy5 and Cy7 intensity images of same field of view.

Fluorescence Image Analysis and Display

Cervical lymph nodes were imaged and analyzed following AVB-620 administration in ear tumor-bearing mice. For each mouse, Cy5 and Cy7 fluorescence images containing both ipsilateral and contralateral cervical lymph nodes were collected and used to make FR images by dividing the Cy5 image by the Cy7 image using the imaging processing program ImageJ (36).

For displaying the FR images, the exposure-corrected Cy5 wavelength fluorescence image was divided by the exposure-corrected Cy7 emission wavelength image and multiplied by 15 so that the values for the FR image filled an 8-bit dynamic range and lie between 0 and 255. A lookup table with RGB values assigned for each intensity level was then used to pseudo-color the FR image. Pseudo-color FR images were scaled for fluorescence intensity by multiplying the pseudo-color image by either the average of Cy5 and Cy7 wavelength fluorescence image resulting in images where hue or color represents the FR and brightness represents fluorescence intensity. An example of how images are collected and the FR display is produced from the two individual intensity images is shown (Fig. S2). In some cases, an intensity-weighted pseudo-color FR image was combined with a reflected light image, for display purposes. For FR images of ear tumor superimposed on reflected image, background was removed by applying a minimum intensity threshold of 25% maximum Cy5.

$$\text{Display Ratio Image Value} = 15*(ICy5/TCy5)/(ICy7/TCy7)$$

Where: $ICy5$ and $ICy7$ are Cy5 and Cy7 fluorescence image intensities and $TCy5$ and $TCy7$ are Cy5 and Cy7 exposure times.

An ellipse or polygon region of interest (ROI) was drawn for each cervical lymph node and the individual averaged fluorescence intensities in ROI were measured. If the FR was uniform in lymph node, then the whole node was used for the ROI. If there was a "hotspot" defined as a clearly defined region of higher FR (required to be >5% of the lymph node area) on the imaged lymph node, then the smaller hotspot ROI was chosen for analysis. Average FR values were calculated from each ROI.

Calculated FR and lymph node pathologic status determined from H&E analysis of stained cervical lymph node sections were used to evaluate AVB-620 sensitivity and specificity. The Receiver Operating Characteristic (ROC) curves which plot true positive rate versus false positive rate were then built to determine the sensitivity and specificity of AVB-620. For ROC curve analysis, data were divided into a

binary classification of positives and negatives based on a threshold value for the FR.

True positives, false positives, true negatives, and false negatives were determined by comparing the prediction based on the FR data and threshold values from imaged cervical sentinel lymph nodes with the presence (positive) or absence (negative) of cancer cells determined by the pathologist using H&E stained tissue sections of imaged cervical lymph nodes.

The threshold value was gradually adjusted from low to high values to obtain a full ROC curve from (1, 1) or all positives to (0, 0) or all negatives. In practice, the ROC curve was generated by sorting the data and using threshold values just above the actual FR values for each examined lymph node. An Excel spreadsheet using Boolean logic was used to calculate true positives, false negatives, true negatives and false positives for each point in the ROC curve. Sensitivity was the true positive rate while specificity was one minus the false positive rate.

Histopathology

After imaging, each mouse was euthanized by intracardiac ketamine-xylazine overdose and the cervical lymph nodes were harvested and fixed in 10% buffered formalin. After an overnight formalin fixation, cervical lymph nodes were processed for histology to assess the fluorescence/cancer correlation. Paraffin sections (5 μm) of cervical sentinel lymph nodes were obtained and processed for routine Hematoxylin & Eosin (H&E) staining performed by Zyagen (San Diego, CA) and HistoTox Labs, Inc. (Boulder, CO). Paraffin sections of cervical sentinel lymph nodes were also immunohistochemically stained for cytokeratin, a marker for epithelial malignancy (37,38). For cytokeratin staining, 5 μm paraffin sections were deparaffinized with xylene, cleared in ethanol, incubated with Proteinase K at room temperature, washed in tris-buffered saline (TBS, 3 x 10 min) and incubated for 30 min at room temperature with TBS containing 0.3% hydrogen peroxide to remove endogenous peroxidase activity. After a further rinsing (2 x 5 min) in TBS, tissues were incubated for 1h at room temperature with rabbit anti-cytokeratin antibody (1:100; Cat.# ab9377, Abcam, MA) diluted in blocking solution. Then tissues were rinsed (3 x 10 min) in TBS and incubated for 30 min at room temperature with Envision + rabbit polymer HRP secondary (Dako, CA). Finally, tissues were rinsed (3 x 10 min) in TBS and processed using DAB for colorimetric detection. Stained sections were examined using the LEITZ LABORLUX S light microscope (Leica Mikroskopie & Systeme GmbH,

Wetzlar) and images captured. Histopathological assessment was conducted by a certified anatomic and clinical pathologist at the VA San Diego Health Care System (San Diego, CA) applying standard histopathological criteria. H&E stained cervical lymph node sections were examined blinded using a Nikon Eclipse Microscope (Tochigi Nikon Precision Co., Ltd., Tochigi, Japan).

Results

AVB-620 Structure, Synthesis and Properties

AVB-620 has many novel chemical features incorporated into the structure (Fig. 1A) that are essential for *in vivo* cancer imaging applications and drug development. The peptide backbone utilizes an asymmetric ACPP comprised of a poly-D-arginine 8-mer (r8) CPP and a poly-D-glutamate 5-mer (e5) masking sequence connected with a PLGC(Me)AG MMP substrate, compared to symmetric (r9)(e9) ACPPs that have been previously described (34,39). In addition to making the peptide smaller, the asymmetric peptide has higher water solubility when labeled with fluorescent dyes and is positively charged compared to negatively charged (r9)(e9) dye labeled molecules at physiological pH. AVB-620 has a far-red fluorescent Cy5 FRET donor moiety conjugated adjacent to the r8 CPP via a thioether linkage made from D-cysteine and a NIR Cy7 FRET acceptor moiety attached to the amino terminus. These indocarbocyanine dyes were selected due to their high water solubility, high molar extinction coefficients, long wavelength excitation and emissions (650–800 nm), and spectral overlap which is favorable for FRET. Finally, a ~2K mPEG moiety was introduced via an orthogonal conjugation chemistry forming a stabilized phenyl oxime from reaction of newly incorporated unnatural amino acid *p*-acetylphenylalanine and mPEG oxyamine. The use of this biocompatible conjugation handle enables the efficient addition of the 3 different moieties to peptide without need for protection and deprotection steps of cysteines as previously reported (34). The combined chemical moieties give AVB-620 high water solubility, > 100 mg/mL, which is important for IV formulation and drug development.

Absorbance and Protease-activated FRET

The AVB-620 absorbance spectrum shows two peaks characteristic of Cy5 and Cy7 maxima at ~650 and ~750 nm respectively (Fig. 1B). From highly purified material and corrected for water content, molar extinction coefficients of 281,000 and 222,000 $M^{-1}cm^{-1}$ were determined in 80/20 phosphate buffered saline/acetonitrile, pH 7.4 at 650 and 750 nm respectively.
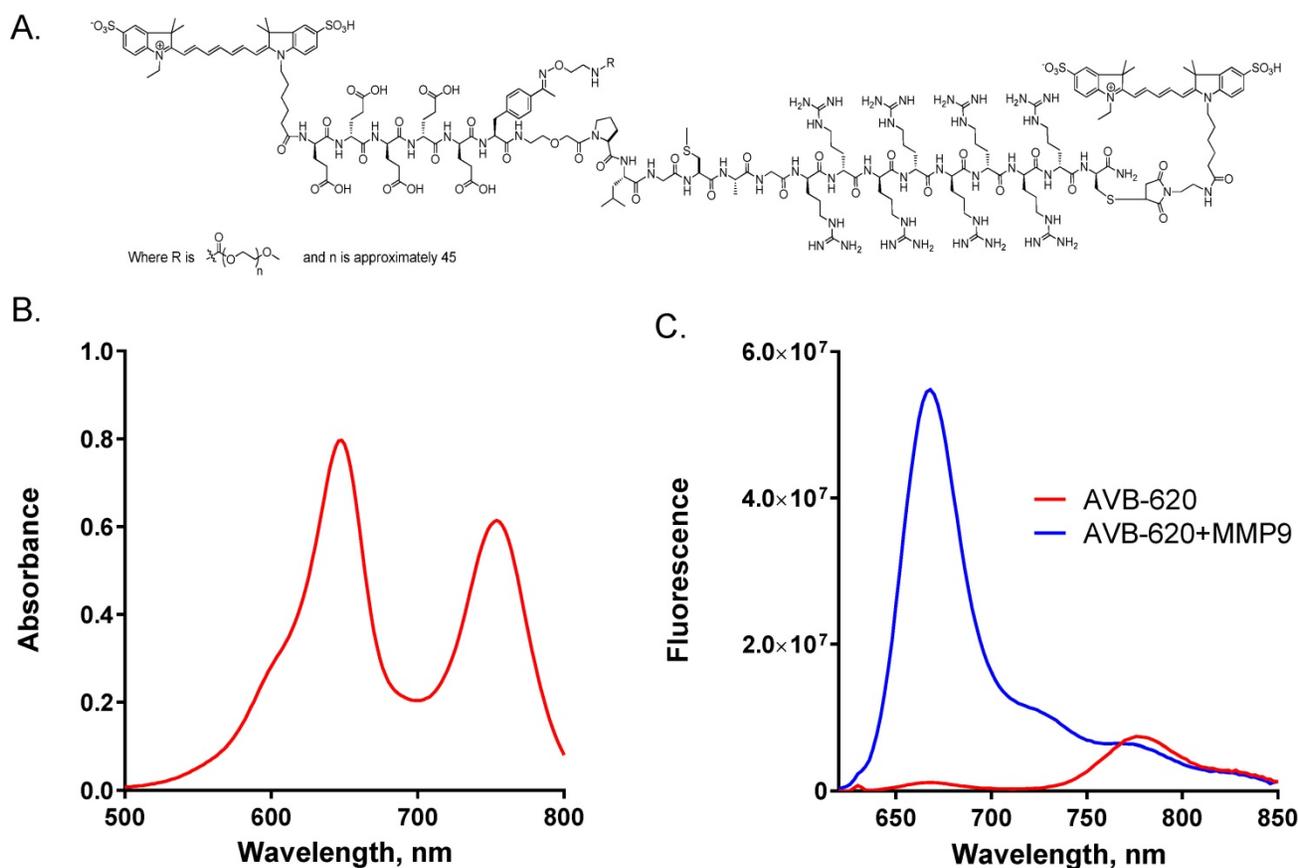
Figure 1. AVB-620 structure, absorbance and fluorescence properties. (A) Structure of AVB-620. **(B)** Absorbance spectrum of 17.5 µg/mL AVB-620 in 80/20 PBS/acetonitrile from 500-800 nm. **(C)** AVB-620 fluorescence emission spectrum in TCNB buffer using 630 nm excitation and an emission wavelength range of 620-850 nm (red trace). Addition of MMP9 hydrolyzes AVB-620, disrupting FRET between Cy5 and Cy7 dyes, and results in large fluorescence change (blue trace). Representative spectra are shown from six experiments.

AVB-620 was designed to utilize FRET from Cy5 donor to Cy7 acceptor in the intact molecule. In the putative ACPP U-shaped conformation (14), the fluorophores are expected to be in close proximity which is a requirement for efficient FRET. For this mechanism, the Cy5 donor fluorescence should be greatly quenched and the Cy7 acceptor would have increased sensitized emission, when exciting at wavelengths corresponding to Cy5 absorbance. AVB-620 stock solutions were prepared from lyophilized solid in TCNB buffer. Fluorescence spectra collected using 630 nm light to excite Cy5 demonstrate a high amount of energy transfer with Cy5 being highly quenched (~98%) and with sensitized emission from Cy7 (Fig. 1C, red trace). The average Cy5/Cy7 FR for intact AVB-620 was a very low 0.13. Reaction of AVB-620 with either MMP9 or proteinase K to hydrolyze the substrate resulted in 100% AVB-620 cleavage and a very large increase in Cy5 fluorescence (59-fold ± 8 SEM), which is much greater than the ~10-fold value for previously reported ratiometric symmetric r9e9 ACPPs (34,39). In addition, the sensitized Cy7 fluorescence decreased ~20%, resulting in an average Cy5/Cy7 FR after

cleavage of 9.26 (Fig. 1C, blue trace). The reduction in 780 nm emission from disrupted FRET is limited by the Cy5 emission at these wavelengths. The great Cy5 enhancement after cleavage results in some residual emission at the Cy7 emission maximum of ~780 nm (~5% of Cy5 emission maximum). The mean FR change upon protease cleavage from six experiments was 73-fold (± 8 SEM), which is greater than the ~30-40-fold reported for previous ratiometric agents (34, 39).

In vitro enzyme kinetics of AVB-620 hydrolysis

AVB-620 has an activating cleavage substrate site (PLG/C(Me)AG) that was designed to be hydrolyzed by MMP2 and MMP9 (14). Therefore, we measured the kinetic parameters of AVB-620 cleavage first by recombinant human MMP2 and MMP9 using a titration of AVB-620 into a fixed concentration of enzyme. To prevent inner filter artifact due to absorbance of the AVB-620, concentration was limited to a maximum of 10 µM in this assay. In that concentration range, the rate of AVB-620 cleavage was essentially linear with respect to [AVB-620]. Therefore, it was clear that K_m was much larger than

10 μM. For this reason, we were not able to derive k_{cat} and K_m separately from these titrations. However, we did derive a combined k_{cat}/K_m, as the slope of velocity versus AVB-620 concentration. AVB-620 was cleaved efficiently by both human MMP2 and MMP9 with k_{cat}/K_m of 213,000 ± 25,000 and 152,000 ± 21,000 M^{-1} sec^{-1} respectively at 37 °C. A control ACPP peptide contained the cleavage substrate site synthesized with unnatural D-amino acids instead of the natural L-amino acids. Proteases should not cleave D-amino acid peptides. In fact, under conditions in which AVB-620 was substantially cleaved by MMP2 or MMP9 no cleavage of the control D-amino acid ACPP by either MMP2 or MMP9 was detected (data not shown).
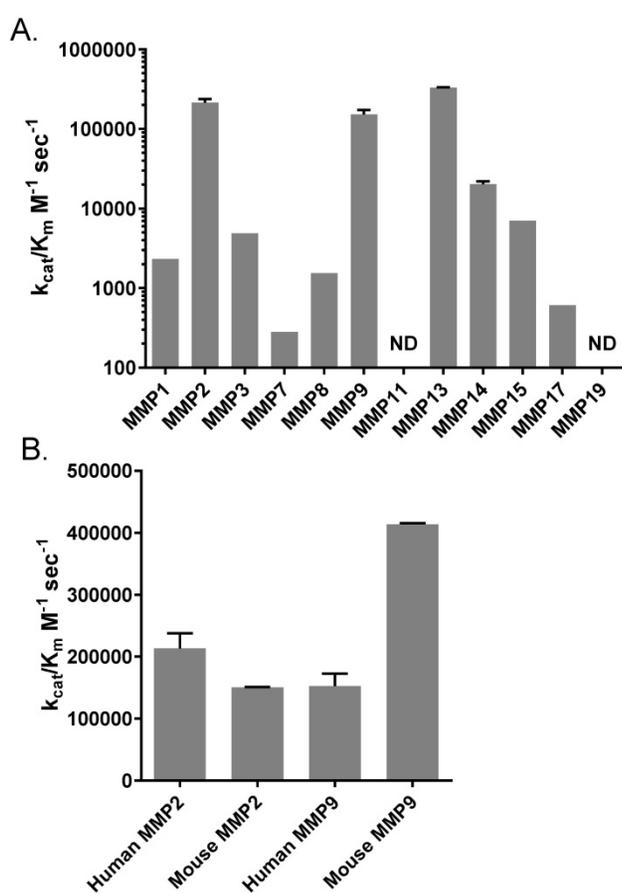
Figure 2. Profiles of MMP cleavage of AVB-620. (A) Catalytic efficiency of a panel of MMPs for cleavage of AVB-620. **(B)** Catalytic efficiency of human MMP2 and MMP9 versus mouse MMP2 and MMP9. Error bars are standard deviations. ND = not detectable.

We were also interested in a profile of AVB-620 cleavage activity for a broad panel of MMPs that may be present in some or many tumor environments (40–42). Using a panel of recombinant human MMPs or MMP catalytic domains we determined k_{cat}/K_m for these MMPs (Fig. 2A). Most tested MMPs exhibited some activity, except for MMP11 and MMP19 which

had no detectable activity. But activity varied widely from a low of 280 M^{-1} sec^{-1} for MMP7 to a high of 388,000 M^{-1} sec^{-1} for MMP13 (note the log scale), a value that is significantly higher than that of MMP2 or MMP9 ($P < 0.001$ and $P < 0.0001$ respectively by 1 way ANOVA, Tukey's multiple comparisons test). In fact, MMP2, MMP9 and MMP13 stand out with high catalytic efficiencies. The next most efficient MMP was MMP14 with k_{cat}/K_m = 20,300 M^{-1} sec^{1}.

Since our *in vivo* preclinical imaging studies were conducted in mice, we also measured the catalytic efficiency of mouse MMP2 and MMP9 and compared them to their human counterparts. The catalytic efficiency of mouse MMP2 was similar to that of human MMP2 and MMP9 with k_{cat}/K_m ~ 200,000 M^{-1} sec^{-1}, but mouse MMP9 had a higher catalytic efficiency with k_{cat}/K_m = 413,000 M^{-1} sec^{-1} (Fig. 2B). Based on these enzymatic activities mouse tumors expressing at least MMP2 and MMP9 should be good models for humans. And while mouse MMP9 cleavage rate is modestly faster, both human enzymes still cleave AVB-620 efficiently, supporting that AVB-620 would also be active in humans. This conclusion is further supported by AVB-620 cleavage in human tumor homogenates (see below, Fig. S5 and Fig. 7).

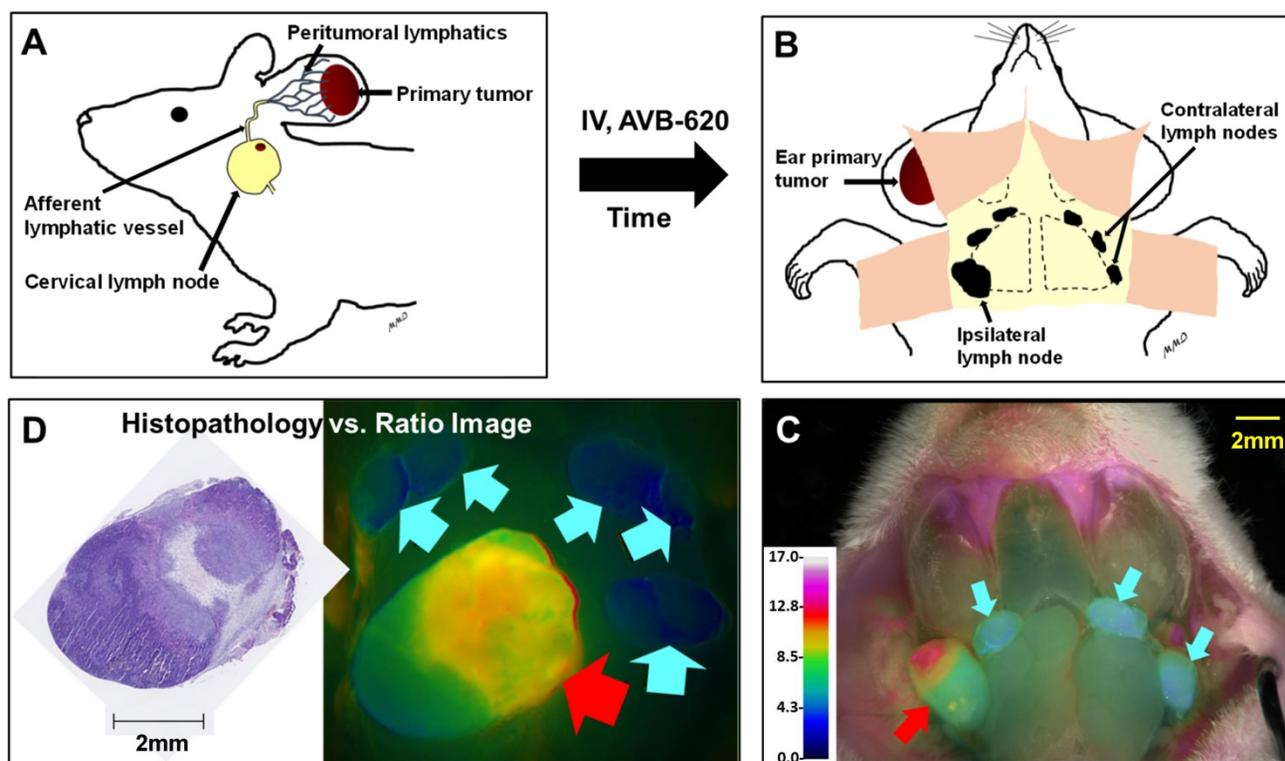### *In vivo* diagnostic imaging in murine metastatic lymph node models

To evaluate AVB-620's ability to be activated *in vivo* and visualize breast cancer in lymph nodes, two murine models of metastatic breast cancer to lymph nodes were used. A schematic of the experimental protocol is shown (Fig. 3). Cancer cells were implanted in ear of immunocompetent mice and after ~2 weeks metastasize to cervical lymph nodes (Fig. 3A). AVB-620 was administered and 3-6 h later the mice were anesthetized and cervical lymph nodes were surgically exposed, and fluorescently imaged (Fig. 3B&C). Finally, the imaged lymph nodes were removed, processed for H&E pathology assessment, and imaging and pathology results were compared (Fig. 3D). In the first model, 30 female BALB/c mice bearing metastatic 4T1 breast cancer tumors on the ear pinna were dosed IV via tail vein injection with AVB-620 (6 nmol). The imaging dose was established from studies using 2 to 24 nmol/mouse. The 6 nmol dose produced the largest FR difference between malignant and non-malignant lymph nodes, while still providing acceptable Cy5 and Cy7 fluorescence intensity signal-to-background. Pre-surgical fluorescence imaging of dorsal, anterior view of mouse (including primary tumor implanted in ear) and surgically exposed cervical lymph nodes were performed. A representative black and white image

with and without superimposed FR images is shown (Fig. 4A). The images show that the pathology-confirmed primary tumor has high FR and intensity compared to rest of exposed body. After surgery, FR images of 60 lymph nodes were analyzed and compared to gold standard H&E histopathology to assess imaging accuracy. The results are shown (Fig. 4B). The diagnostic sensitivity and specificity were 96% and 100% respectively using FR thresholds from 6.7-7.4, which produced the highest overall accuracy of 98%. The ROC curve is shown (Fig. S3A) and a representative FR image of exposed cervical lymph node area is shown (Fig. 4C).

The kinetics and stability of the FR difference between cancer-free and metastatic lymph nodes was evaluated from 1-48 h after dosing AVB-620 and is shown (Fig. 4D). A significant FR difference was observed at 1 h ($P < 0.02$, t-test) but was greatest at 3-6 h and was stable to 24 h. This usable diagnostic time window is much greater than the AVB-620 plasma half-life in mice of 0.24 h (Fig. S4A). At 48 h the FR difference is still significant ($P < 0.01$, t-test) but reduced primarily due to a FR increase in the uninvolved lymph nodes. This result is very different than r9e9 ratiometric ACPPs which appear to have maximum contrast at 2 hours and show no difference

between malignant and non-malignant tissue at 24 hours (34).

An analogous imaging study was performed using 24 female immunocompetent C57BL/6 mice bearing a syngeneic, polyoma middle T subclone (8119) breast cancer tumor on ear. The imaging was done 6 h after AVB-620 administration and a total of 48 lymph nodes were analyzed. A representative pre-surgical black and white image with and without superimposed FR image is shown (Fig. 5A). The images show that the pathology-confirmed tumor has high FR and intensity compared to rest of exposed body, like those from 4T1 tumor study. The FR values from cancerous nodes were completely separated from those of uninvolved nodes and the sensitivity and specificity were both 100% for FR thresholds from 5.76 to 6.61 (Fig. 5B). A representative FR image of an exposed cervical lymph node area is shown (Fig. 5C). A total of 108 lymph nodes (pathology determined 46 positive and 62 negative) were evaluated in the two models. In five cases, the FR was high but the initial H&E result was negative for cancer. For these nodes, additional sectioning was performed and in all cases cancer was found in these additional sections, indicating that pathology missed these true positives and use of imaging data increased detection of true positives 12%.

Figure 3. Schematic of metastatic lymph node model and *in vivo* diagnostic imaging protocol. (A) Breast cancer cells are implanted into mouse ear and metastasize to cervical lymph nodes. AVB-620 is administered via tail vein injection and 3-6 h later the cervical area is surgically exposed **(B)** and the lymph nodes are imaged. A fluorescence ratio (FR) image is displayed superimposed on reflected white light image using an RGB scale where high ratio is red and low ratio is blue **(C)**. The red arrow indicates a cancer-positive cervical lymph node and cyan arrows indicate cancer-negative one as determined by histopathology. The nodes are then surgically removed and processed for H&E histopathological analysis. **(D)** The pathology results are directly compared to image ratio values.
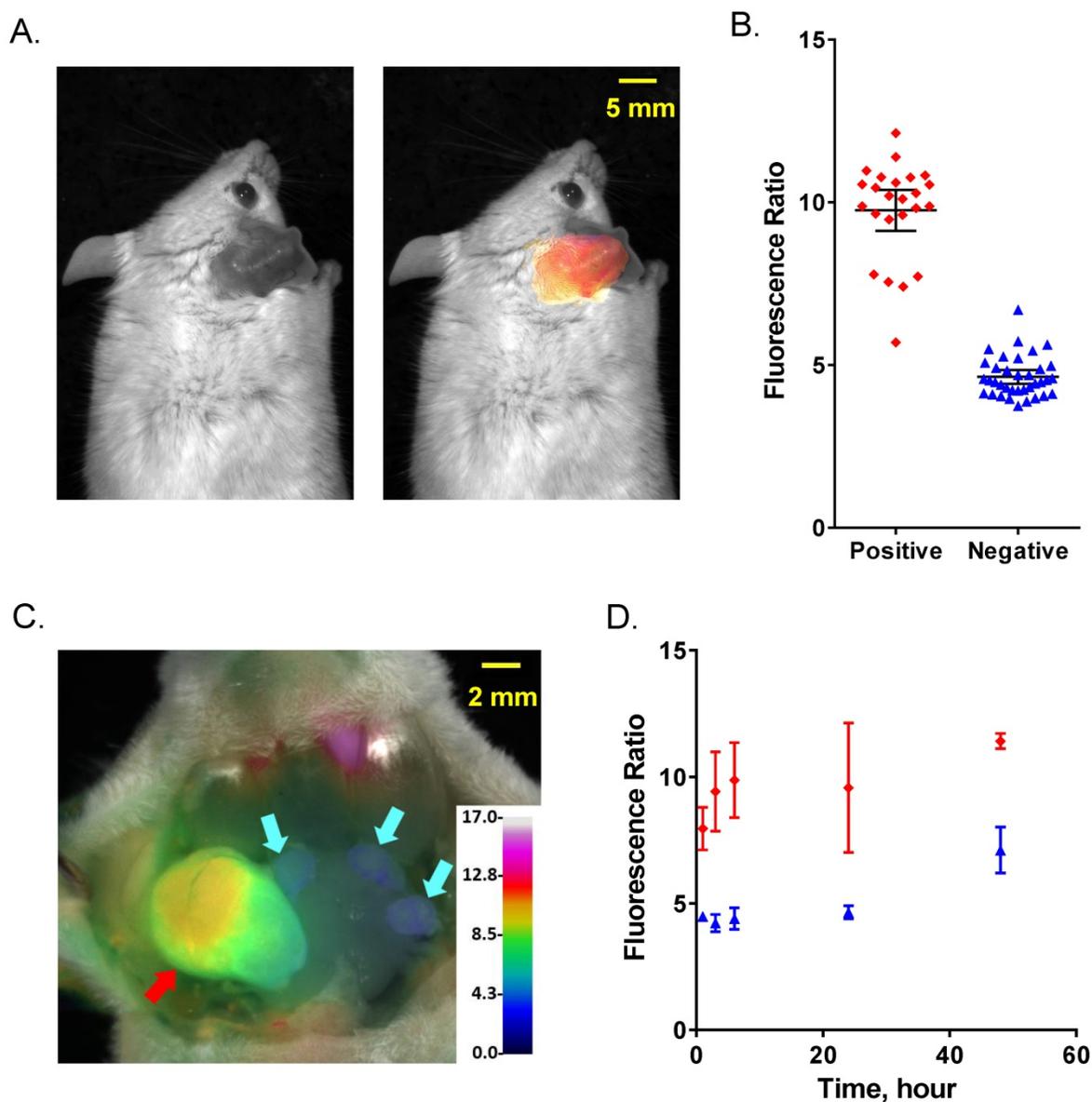
Figure 4. Comparison of FR imaging and histopathology using 4T1 metastatic lymph node model. (A) Representative black and white dorsal mouse image with (right) and without (left) FR image superimposed showing high ratio in primary tumor in mouse ear. **(B)** AVB-620 generated FR values for cervical lymph nodes grouped by cancer status as determined from H&E histopathology. Cancer-positive (red diamonds) and cancer-negative (blue triangles) lymph nodes are shown. The black lines show the mean ± 95% confidence level. **(C)** Representative ratio image of exposed lymph nodes blended with reflected light image. The ratio is displayed using an RGB scale where high ratio is red and low ratio is blue. Red and cyan arrows indicate cancer positive and negative lymph nodes respectively. **(D)** Kinetics of AVB-620 *in vivo* diagnostic ratio signal from 1 to 48 h after dosing. Cancer-positive (red diamonds) and cancer-negative (blue triangles) lymph nodes are shown. The error bars are standard deviations.

While the *in vivo* diagnostic studies provided yes/no results for each ROI, imaging can provide spatial information within regions or tissues of interest. To evaluate the spatial relationship of the FR signal and the location of cancer within a tissue sample, we imaged putative metastatic lymph nodes and adjacent tissue and then paraffin embedded the tissue while retaining the same orientation and sectioned in the block to generate oriented samples that would match the *in vivo* images. Comparison of the *in vivo* images with the H&E histopathology and cytokeratin immune-histopathology demonstrated

that the high FR corresponded with the cancerous portion of the tissue in both 4T1 and PyMT models. Representative examples are shown (Fig. 6). The 4T1 example (Fig. 6A-C) shows a cancerous lymph node extension which facilitates identification and confirmation of the same orientation between the *in vivo* image and the histopathology sections.

## Rodent safety, toxicology, metabolism, and estimated human dose

No abnormal behaviors or toxicity were observed during AVB-620 *in vivo* murine imaging

studies, (N>200). Exploratory tolerability at higher doses was evaluated in female BALB/c mice (N=6) at 30 and 60-fold higher concentrations (53 and 106 mg/kg) and compared with vehicle controls (N=6), with no adverse observations. More comprehensive non-GLP and GLP single-dose toxicological evaluations which included clinical chemistry, tissue histopathology and toxicokinetics (TK), were done in male and female rats with 2 day and 14 day recovery. At the highest dose tested (N=30), no adverse effects were observed, producing an NOAEL of 100 mg/kg in rats. At this high dose, potential neurological effects were assessed with GLP modified Irwin test and no significant effects were observed. Scaling for body surface area, this is a >110-fold dose margin over the

mouse imaging dose. Importantly, this dose exceeds that which produced 5/5 mouse deaths for r9e9 symmetric ACPP (43). When tested at the same dose, AVB-620 was tolerated in mice and no deaths were observed, which demonstrates improved safety. Based on measured female rat TK AUC (data not shown), this dose produces a >230-fold exposure margin above that of the mouse imaging studies. Using standard allometric scaling (44), the mouse imaging dose is estimated to be equivalent to ~9 mg in people while the rat NOAEL gave an estimated human dose of 1044 mg. Thus, the rat NOAEL provides a >100-fold dose safety margin over estimated human dose.
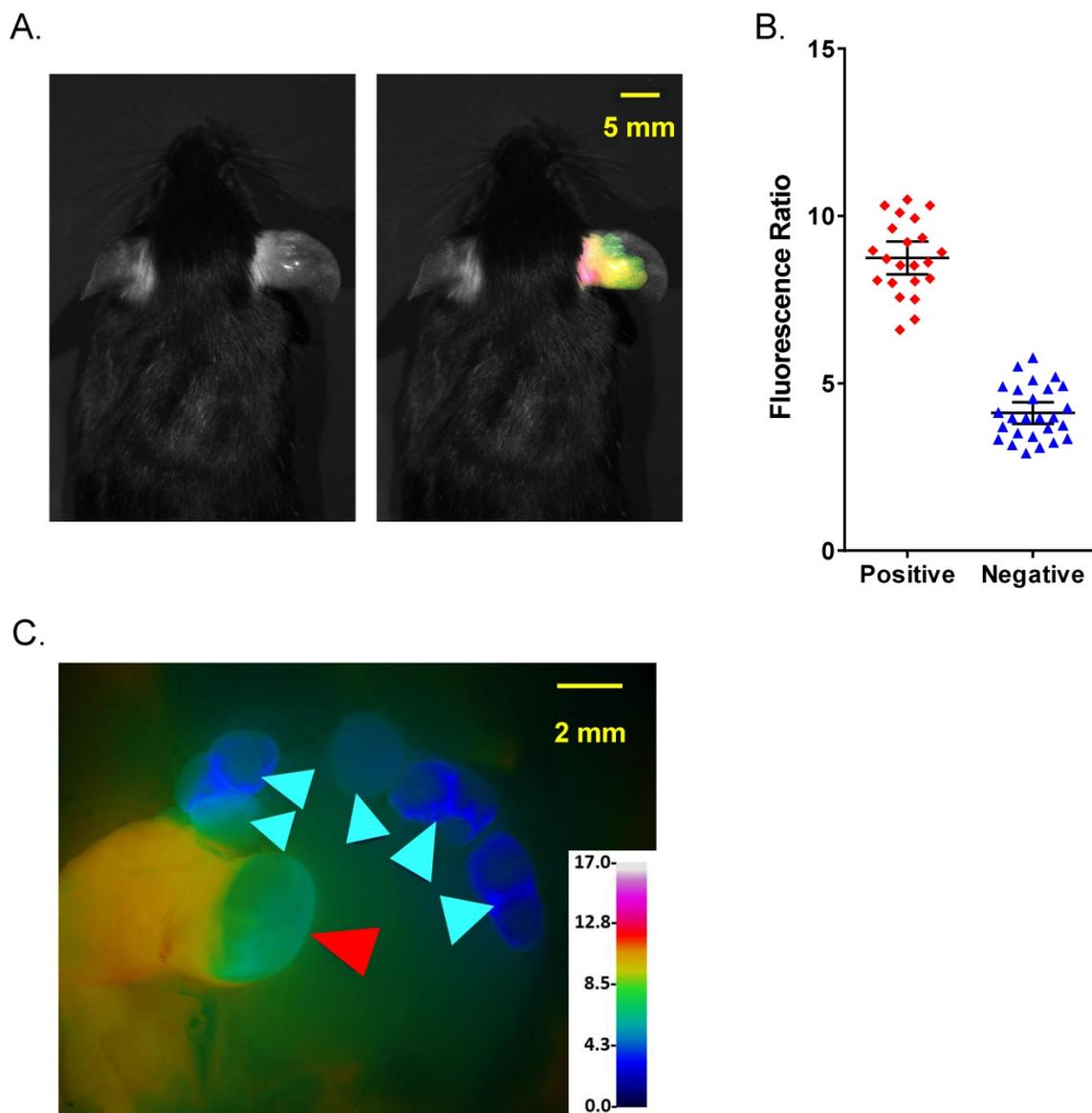
Figure 5. Comparison of fluorescence imaging and histopathology using PyMT metastatic lymph node model. (A) Representative black and white dorsal mouse image with (right) and without (left) FR image superimposed showing high ratio in primary tumor in mouse ear. **(B)** AVB-620 generated FR values for cervical lymph nodes grouped by cancer status determined using H&E histopathology. Cancer-positive (red diamonds) and cancer-negative (blue triangles) lymph nodes are shown. The black lines show the mean ± 95% confidence level. **(C)** Representative FR image of lymph nodes is displayed using an RGB scale where high ratio is red and low ratio is blue. Red and cyan arrowheads indicate cancer positive and negative lymph nodes respectively.
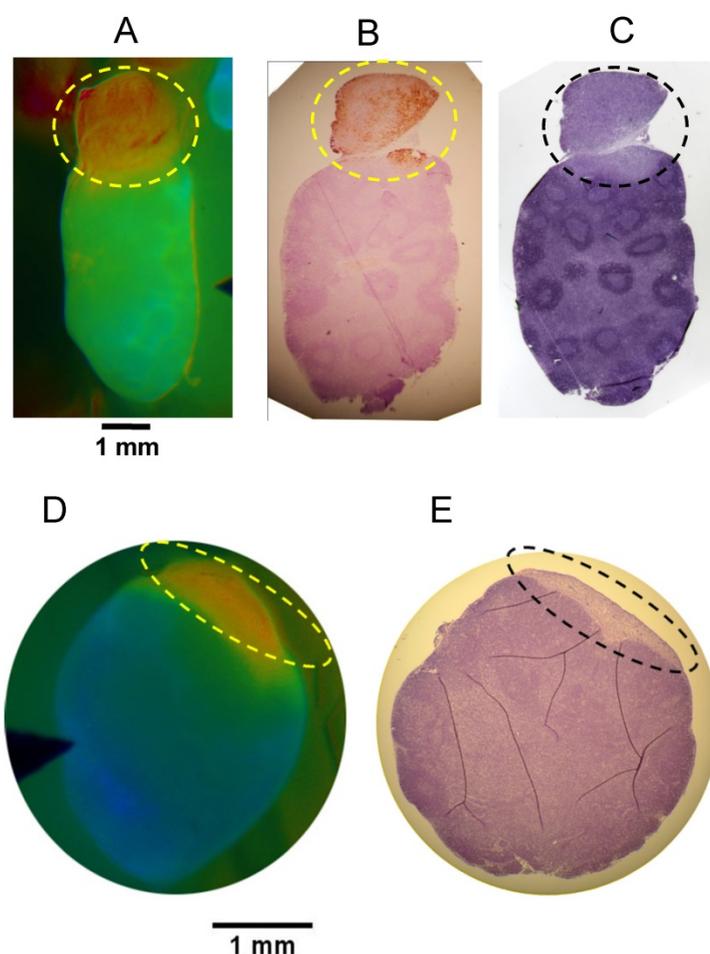
Figure 6. Oriented Fluorescence Imaging and Histopathology. Representative mouse *in vivo* FR images and corresponding oriented histopathology sections of metastatic cervical lymph nodes in mice administered AVB-620. Consecutive paraffin sections of each lymph node were processed for cytokeratin and/or H&E staining. **(A)** *in vivo* Cy5/Cy7 FR image of the 4T1 metastatic lymph node. **(B)** cytokeratin stained and **(C)** H&E stained. Images D & E are representative data from PyMT model. **(D)** AVB-620 *in vivo* Cy5/Cy7 FR image and **(E)** H&E stained lymph node. Ratio images used an RGB scale where red is high ratio and blue is low ratio. The dotted oval outlines the region of cancer invasion.

Rat TK demonstrated high AVB-620 exposure and *in vivo* hydrolysis metabolites generated from protease substrate cleavage. The observed poly-arginine-Cy5 containing metabolite(s) had the same HPLC retention time as synthesized metabolite standard with Cys(Me)AG attached to poly-arginine-Cy5 (data not shown), consistent with MMP generated metabolites. The same poly-arginine-Cy5 metabolite(s) was also observed in mice. To assess compound stability in circulating blood, AVB-620 was incubated with plasma from rat and humans at 37 °C and assayed with HPLC. The results show that AVB-620 was substantially more stable in human plasma compared to that of rats (only 16% loss after 6 hours versus 69%, Fig. S4B), supporting human translation.

## *In vitro* diagnostic AVB-620 proteolysis in human breast cancer tissue

We acquired 25 matched pairs of malignant breast cancer and healthy adjacent tissue samples, each from the same breast cancer patient, through CHTN. There were no exclusion restrictions on the cancer type, stage, or receptor status. The patients ranged from 38-77 years in age and all had invasive breast carcinoma. Seventeen had ductal carcinoma, six had lobular carcinoma (three had both) and five were undetermined. Two patients were triple negative for growth factor receptors and three had no information about receptor status. The rest were positive for growth factor receptors. Homogenates prepared from all matched tissues were assayed for AVB-620 proteolytic activity and for the presence of MMPs. For each tissue sample pair, malignant tissue always showed higher proteolytic cleavage activity than adjacent healthy tissue (Fig. 7). The mean proteolytic activity of malignant tissue (0.43 nM/min) was significantly higher ($P < 0.0001$; paired T-test) compared to that of healthy matched control sample (0.18 nM/min) yielding therefore an average difference of 2.4-fold between pairs (Fig. 7B).

Systematically varying the threshold, the ROC curve yielded an optimal accuracy of 92% with sensitivity of 96% and specificity of 88% (Fig. 7C). An analogous tissue homogenate study was performed with mouse 4T1 primary tumors grown in mammary fat pad and adjacent muscle as non-malignant control. The mouse tumor tissue hydrolyzed AVB-620 ~2-fold faster than adjacent muscle, similar to that from malignant human tumors (Fig. S5). Homogenates from a random subset of the matched pairs with sufficient tissue were also assayed in a gelatin zymogram gel that is sensitive to MMP2 and MMP9 activity (Fig. 8A). This gel clearly showed elevated levels of pro and activated forms of MMP2 and MMP9 in the tumor samples relative to the non-malignant samples for each pair tested. The gel shown is of three representative pairs but additional gels (not shown) gave similar results.

Active MMP2 concentration in these samples was estimated from zymogram gels based on a standard curve of active recombinant MMP2 run with the samples using ImageJ densitometry. The three tumor samples gave an average active MMP2 concentration in the tumor tissue of 6.9 nM. The normal samples had no detectable active MMP2 (sensitivity limit <0.2 nM). Qualitatively, proMMP2 and pro or active MMP9 also had higher activity in cancerous tissue. However, MMP9 concentrations could not be quantified because it has multiple bands that could not conclusively be identified and some of these bands overlap with proMMP2 (Fig. 8A).
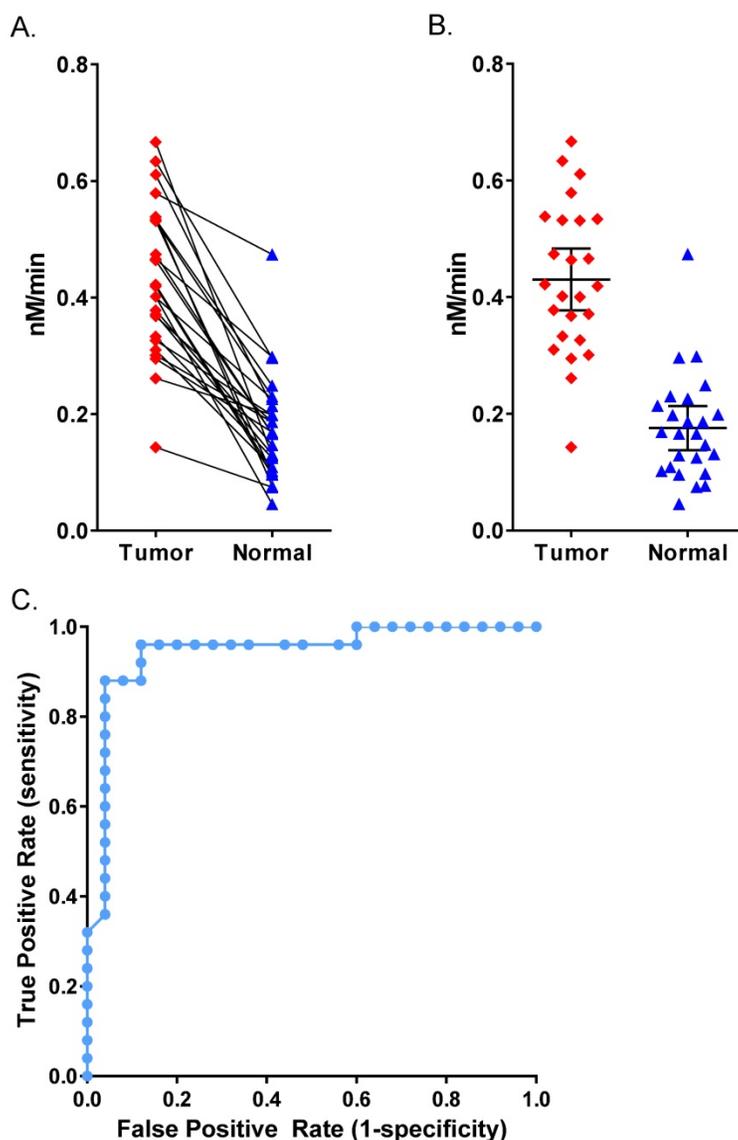
Figure 7. Human Patient Breast Cancer Malignant Tumor Tissue. (A) AVB-620 cleavage rate, nM cleaved per minute, in 25 paired human breast cancer patient tissue homogenates. Cancer-positive tumor tissue (red diamonds) and cancer-negative adjacent tissue (blue triangles) are shown. Paired samples are connected by lines. Paired t-test gave $P < 0.0001$ for significant difference between tumor and normal. (B) Scatter plot of the same data with mean ± 95% confidence level. (C) ROC curve for AVB-620 cleavage rate detection of tumor versus normal tissue.
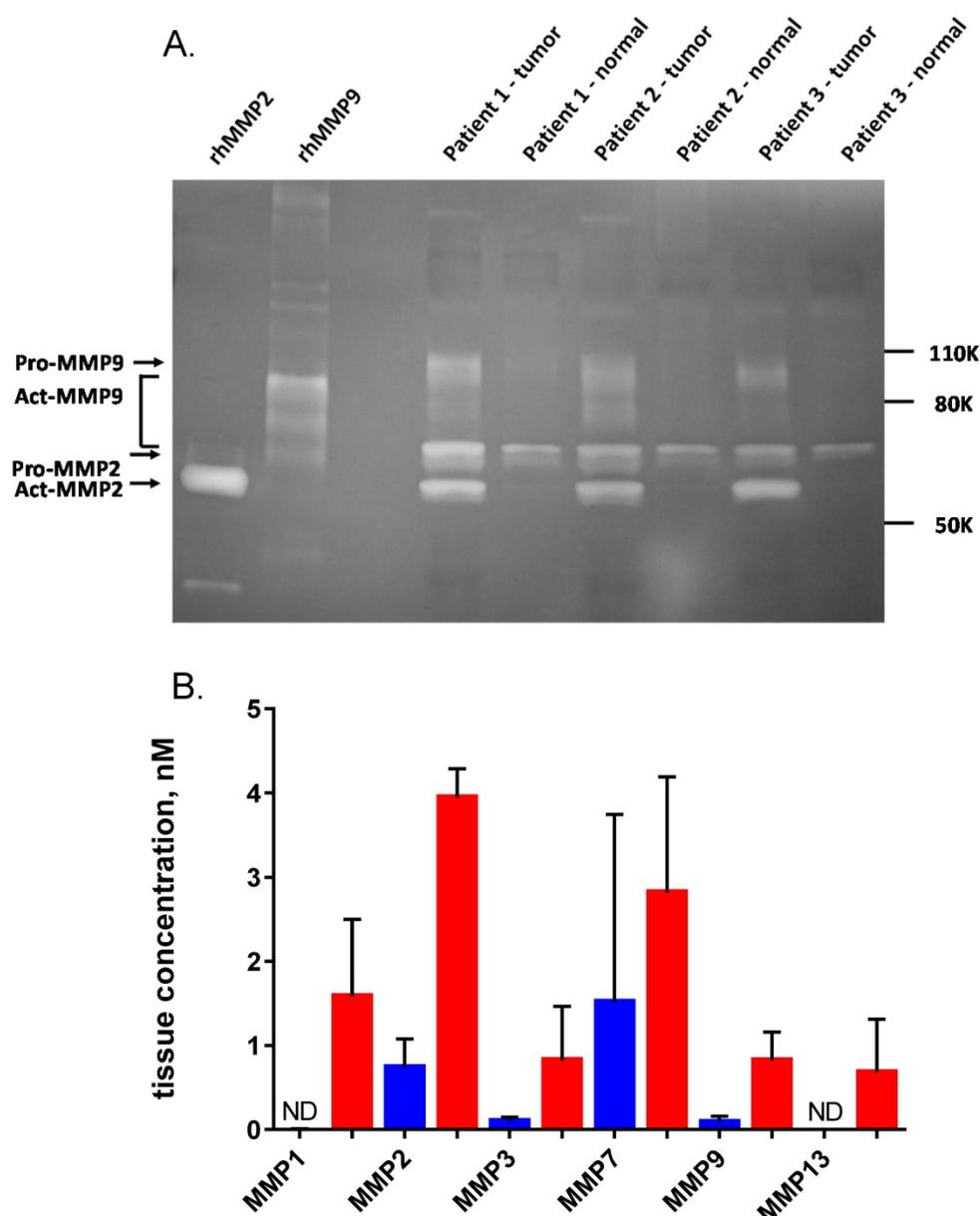
Figure 8. Quantification of MMPs in non-malignant breast tissue and tumor homogenates. (A) Homogenates from three representative human breast cancer samples and paired normal tissue, selected from the 25 patients in Fig. 7 were analyzed on a 10% gelatin zymogram. Recombinant active MMP2 and MMP9 were used as standards (2 ng per lane). **(B)** ELISA quantification of six MMPs in five representative human breast cancer samples (red) and paired normal tissue (blue), including the three pairs shown in panel A. Error bars are standard deviations. ND = not detectable.

Five matched pairs of human tissue homogenate samples were also analyzed for MMP protein using a multiplexed ELISA system (Fig. 8B). The six MMPs that were measured were all increased on average in the tumor relative to the normal adjacent tissue, however the increase for MMP7 was not significant. Mean MMP2 concentration by ELISA in the tumor samples was 3.9 nM, consistent with the concentration of active MMP2 estimated by zymogram.

Discussion

Protease-activated imaging agents utilize disease biochemistry to generate localized contrast and are a promising class of probes for *in vivo* visualization of cancer (14, 15). With the goal of providing surgeons improved intra and perioperative cancer visualization, we have developed a novel and improved IV administered ratiometric protease-activatable fluorescent peptide dye conjugate, AVB-620, designed and optimized for sensitive and accurate cancer detection and visualization, and shown here for breast cancer.

The peptide backbone utilizes a new asymmetric ACPP with a MMP substrate and incorporating three orthogonal chemical handles for efficient bio-conjugation of two fluorescent dyes and a mPEG

moiety. The substrate was selected for its ability to be hydrolyzed by multiple MMPs that are important in cancer and associated microenvironment tissues. The asymmetric design and mPEG were utilized to reduce molecular size, generate a positively charged molecule at physiological pH and greatly improving water solubility, which is essential for safe and reliable aqueous IV formulations. High solubility is also critical for practical manufacturing scale-up and high dose toxicology studies that are required for human studies and product development. The mPEG group is attached adjacent to the poly-D-glutamate of ACPP so that it is jettisoned after AVB-620 hydrolysis, so as not to interfere with CPP tissue retention activity. AVB-620 utilizes highly efficient FRET between far-red Cy5 and NIR Cy7 fluorescent moieties attached to the peptide core. These dyes were selected for their good chemical and optical properties, which are favorable for FRET and *in vivo* imaging. The wavelengths being mostly beyond the visible spectrum result in low color interference with white light images, and are in the part of the electromagnetic spectrum where tissue absorption and scattering are relatively low.

In vitro characterization using recombinant MMPs demonstrated that targeted MMPs 2, 9, and 14 hydrolyze AVB-620 producing a large ratiometric fluorescence change of ~70-fold, which is greater than previously reported ratiometric ACPP compounds (34). AVB-620 was shown to be a substrate for both mouse and human MMP2 and 9, which is essential for model relevance and in predicting human activity. Interestingly, we discovered that it is also a good substrate for MMP13, also called collagenase 3. This MMP cleaves collagen II, is normally expressed in cartilage and is involved in bone development and remodeling. However, MMP13 also plays a role in cancer progression and it was first cloned from a breast cancer cDNA library (45). MMP13 is expressed in various cancers, including breast, head and neck, melanoma, lung (46) and colorectal (47). MMP13 has substrate specificity that is very similar to that of MMP9 and aligns well with the cleavage site in AVB-620 (48, 49).

AVB-620 with ratiometric fluorescence imaging demonstrated primary tumor visualization and high *in vivo* diagnostic accuracy for detection of cancer positive and negative lymph nodes with sensitivity and specificity both >95% and overall accuracy of 98% in two syngeneic metastatic breast cancer models using immunocompetent mice. Applying this method identified 12% more true positive lymph nodes. This result highlights how AVB-620 imaging can address false negatives inherent in the existing gold-standard histopathology due to limited sampling, while still preserving the ability to confirm fluorescent findings using additional sectioning and histopathology, unlike tissue destructive methods, such as PCR (50). While sectioning an entire tissue sample is theoretically possible, it is not practical. Another optical imaging advantage is high spatial resolution. Comparison of oriented AVB-620 *in vivo* images with histopathology showed excellent correspondence and visualized cancer location within lymph nodes. Lymph node extensions and metastases of approximately 200 microns diameter could be resolved, the lower limit of micro-metastasis definition utilized in clinical breast cancer (51). A diagnostic window between positive and negative lymph nodes was achieved within 1 h and maximal at 3-24 h. Even at 48 h the metastatic lymph nodes had significantly higher FR than uninvolved nodes. This is very different than previously reported ratiometric probes that had no difference between cancer and adjacent tissue at 24 h (34). AVB-620's large useful time window indicates good potential for dosing flexibility in humans and is consistent with ratiometric and tissue retention CPP properties.

The single molecule FRET mechanism generates a discrete and anti-correlated ratiometric fluorescence response where the Cy5 increases and Cy7 signal decreases in concert upon hydrolysis. This is fundamentally different from other dual-fluorophore approaches that employ one as an internal standard on nanoparticles (52) or as separate co-injected molecule (53, 54). While these approaches attenuate artifacts due to bio-distribution, they have shortcomings compared to FRET approach including: lack of an inversely correlated signal that is easier to distinguish from artifacts; complicated readouts that are dependent on variability and degree of fluorophore labeling on particles or proteins; different potential bio-distributions of co-injected standards; and increased chemistry and imaging complexity. The AVB-620 readout reduces many common artifacts that are associated with single intensity fluorescence imaging methods and enables a reliable, absolute threshold value for differentiating cancer from non-cancer tissue, which simplifies comparison across individuals, models, and improves diagnostic performance. To demonstrate this feature, the same FR threshold could be used for both murine metastatic lymph node models, while maintaining high accuracy.

To understand the potential for human translation and relevance of murine breast cancer models, we studied the ability of human breast cancer tissue homogenates to hydrolyze and activate AVB-620. In all cases, tumor homogenates had faster rates of cleavage compared to matched adjacent

non-malignant tissue with on average a 2.4-fold faster ($P < 0.0001$) rate of cleavage. A ROC analysis demonstrated that AVB-620 fluorogenic response accurately predicted whether tissue was malignant or not with a sensitivity of 96% and specificity of 88%. An analogous tissue homogenate activity experiment was done using mouse 4T1 tumors used in the *in vivo* diagnostic imaging study. The absolute AVB-620 hydrolysis rate and relative rate compared to adjacent noncancerous control tissue were essentially the same as was found in the human tissue. These results demonstrate that the collective agent-relevant protease activity in the mouse model was similar to that found in human breast cancer tissues, supporting the model relevance and potential for human translation. In acquiring the human tissue samples, no biological exclusion criteria were used. Patients had a variety of receptor statuses, breast tumor type, cancer stage, grade, sex, and ethnic backgrounds. The higher protease activity in tumor tissue compared to adjacent breast tissue appears to be a general property across all tested breast cancer patients.

Since AVB-620 has been shown to be a substrate for MMP2 and MMP9, we studied the functional activity of these proteases in patient homogenates using gelatin zymography (Fig. 8). As previously reported (27,28), we found that these MMPs have higher activity in tumor samples. The relative amounts of these proteases varied among patients but the combined activity was very consistent and at least one of these MMPs was found to be substantially higher in tumor tissue compared to uninvolved adjacent tissue. This patient heterogeneity further supports use of a substrate that can be activated by multiple proteases that have increased activity in cancer tissue. The protein expression of a broader range of MMPs was studied in these samples with ELISA assays. The same pattern of higher MMP activity in tumor tissue was observed, including MMP2 and MMP9. The MMP2 concentration levels, approximately 5 nM, were similar in both zymography and ELISA assay methods. Expression of MMP13, which was found to have relatively high AVB-620 hydrolysis activity, was observed in human tumor tissue but not in non-malignant adjacent tissue, further supporting a potential role of this MMP in AVB-620's *in vivo* cancer visualization. A ratiometric ACPP with the same protease substrate has been shown to have higher activation in human head and neck squamous cell carcinoma tissue compared to normal tissue (55), supporting the potential of AVB-620 to be useful for additional human cancers.

AVB-620-based fluorescence imaging in breast cancer patients has the potential to aid visualization of primary tumors, satellite lesions, margins, and metastatic lymph nodes in the operating room. It is envisioned that AVB-620 will be used with radioactive lymphatic mapping agents including Tc colloid or Lymphoseek. The approach provides a robust, and accurate readout in animal models and human tissue that support human translation. Clinical utility of AVB-620 will require successfully navigating potential issues that are not fully addressed here. While the *in vitro* human tissue study included a broad range of patients with invasive breast cancer, additional patient heterogeneity from biological variability and treatment is likely. In addition, non-cancer related protease activity, for example from inflammation (56), could cause potentially interfering fluorescence changes. FIGS also has physical constraints that are independent of specific agents. Being a light-based imaging modality, fluorescence has similar limitations to white light visualization including low tissue penetration and significant attenuation due to scattering (3). The larger size of human patients, organs and the thickness of surrounding tissue could result in the decreased ability to visualize malignant tissue compared to mouse models. However, the depth of fluorescence visualization should be equal to or better than that from reflected white light illumination. Tissue resection creates a new surface and visual detection of malignant tissue on this surface is of paramount importance to surgeon and patient.

We have designed and developed AVB-620, a novel and improved ratiometric protease-activatable fluorescent peptide dye conjugate, to enable real-time, intraoperative visualization of cancer in humans. AVB-620 in combination with a fluorescence imaging camera system can visualize tumors and has high diagnostic sensitivity and specificity for determining the lymph node status in metastatic murine breast cancer models. The agent is very well tolerated and the estimated human dose of ~9 mg is more than 100-fold below the NOAEL in rats. *In vitro* homogenate data from human patients support human translation and indicate that this approach could be broadly applicable in breast cancer patients. AVB-620 is currently being studied in a clinical trial which includes imaging of primary tumors, margins, and axillary lymph nodes in breast cancer patients undergoing surgery (57).

Acknowledgments

cancer tissue was acquired from CHTN. Finally, we deeply appreciate and miss our collaborator and mentor Roger Y. Tsien who passed away during the preparation of this manuscript in August of 2016. His impact on this work, science, and us personally cannot be overstated.

Supplementary Material

Supplementary figures.
http://www.thno.org/v07p3369s1.pdf

Competing Interests

MM, JL, AH, AJG, SLC, and JEG are employees of Avelas Biosciences and have company stock and/or stock options. QTN and RYT have company stock. Some results in this paper are included in various issued and pending patents. All work was funded by Avelas Biosciences.

References

1. Moran MS, Schnitt SJ, Giuliano AE, Harris JR, Khan SA, Horton J, et al. Society of Surgical Oncology-American Society for Radiation Oncology consensus guideline on margins for breast-conserving surgery with whole-breast irradiation in stages I and II invasive breast cancer. Ann Surg Oncol. 2014; 21:704–16.
2. Carter CL, Allen C, Henson DE. Relation of tumor size, lymph node status, and survival in 24,740 breast cancer cases. Cancer. 1989; 63:181–7.
3. Allison RR. Fluorescence guided resection (FGR): A primer for oncology. Photodiagnosis Photodyn Ther. 2016; 13:73–80.
4. Vahrmeijer AL, Hutteman M, van der Vorst JR, van de Velde CJH, Frangioni JV. Image-guided cancer surgery using near-infrared fluorescence. Nat Rev Clin Oncol. 2013; 10:507–18.
5. Mondal SB, Gao S, Zhu N, Liang R, Gruev V, Achilefu S. Real-time fluorescence image-guided oncologic surgery. Adv Cancer Res. 2014; 124:171–211.
6. Stummer W, Pichlmeier U, Meinel T, Wiestler OD, Zanella F, Reulen H-J, et al. Fluorescence-guided surgery with 5-aminolevulinic acid for resection of malignant glioma: a randomised controlled multicentre phase III trial. Lancet Oncol. 2006; 7:392–401.
7. Korb ML, Hartman YE, Kovar J, Zinn KR, Bland KI, Rosenthal EL. Use of monoclonal antibody-IRDye800CW bioconjugates in the resection of breast cancer. J Surg Res. 2014; 188:119–28.
8. Terwisscha van Scheltinga AGT, Dam GM van, Nagengast WB, Ntziachristos V, Hollema H, Herek JL, et al. Intraoperative Near-Infrared Fluorescence Tumor Imaging with Vascular Endothelial Growth Factor and Human Epidermal Growth Factor Receptor 2 Targeting Antibodies. J Nucl Med. 2011; 52:1778–85.
9. Warram JM, de Boer E, Sorace AG, Chung TK, Kim H, Pleijhuis RG, et al. Antibody-based imaging strategies for cancer. Cancer Metastasis Rev. 2014; 33:809–22.
10. Rosenthal EL, Warram JM, de Boer E, Chung TK, Korb ML, Brandwein-Gensler M, et al. Safety and Tumor Specificity of Cetuximab-IRDye800 for Surgical Navigation in Head and Neck Cancer. Clin Cancer Res Off J Am Assoc Cancer Res. 2015; 21:3658–66.
11. van Dam GM, Themelis G, Crane LMA, Harlaar NJ, Pleijhuis RG, Kelder W, et al. Intraoperative tumor-specific fluorescence imaging in ovarian cancer by folate receptor-α targeting: first in-human results. Nat Med. 2011; 17:1315–9.
12. Fidel J, Kennedy KC, Dernell WS, Hansen S, Wiss V, Stroud MR, et al. Preclinical Validation of the Utility of BLZ-100 in Providing Fluorescence Contrast for Imaging Spontaneous Solid Tumors. Cancer Res. 2015; 75:4283–91.
13. Swanson KI, Clark PA, Zhang RR, Kandela IK, Farhoud M, Weichert JP, et al. Fluorescent cancer-selective alkylphosphocholine analogs for intraoperative glioma detection. Neurosurgery. 2015; 76:115-123; discussion 123-124.
14. Jiang T, Olson ES, Nguyen QT, Roy M, Jennings PA, Tsien RY. Tumor imaging by means of proteolytic activation of cell-penetrating peptides. Proc Natl Acad Sci U S A. 2004; 101:17867–72.
15. Whitley MJ, Cardona DM, Lazarides AL, Spasojevic I, Ferrer JM, Cahill J, et al. A mouse-human phase 1 co-clinical trial of a protease-activated fluorescent probe for imaging cancer. Sci Transl Med. 2016; 8:320ra4.
16. Luby BM, Charron DM, MacLaughlin CM, Zheng G. Activatable fluorescence: From small molecule to nanoparticle. Adv Drug Deliv Rev. 2016;
17. Urano Y, Sakabe M, Kosaka N, Ogawa M, Mitsunaga M, Asanuma D, et al. Rapid cancer detection by topically spraying a

18. Blum G, Weimer RM, Edgington LE, Adams W, Bogyo M. Comparative assessment of substrates and activity based probes as tools for non-invasive optical imaging of cysteine protease activity. PLoS One. 2009;4:e6374.
19. Bremer C, Tung CH, Weissleder R. In vivo molecular target assessment of matrix metalloproteinase inhibition. Nat Med. 2001; 7:743–8.
20. Lee S, Ryu JH, Park K, Lee A, Lee S-Y, Youn I-C, et al. Polymeric nanoparticle-based activatable near-infrared nanosensor for protease determination in vivo. Nano Lett. 2009; 9:4412–6.
21. Lin X, Xie J, Zhu L, Lee S, Niu G, Ma Y, et al. Hybrid ferritin nanoparticles as activatable probes for tumor imaging. Angew Chem Int Ed Engl. 2011; 50:1569–72.
22. Baik FM, Hansen S, Knoblaugh SE, Sahetya D, Mitchell RM, Xu C, et al. Fluorescence Identification of Head and Neck Squamous Cell Carcinoma and High-Risk Oral Dysplasia With BLZ-100, a Chlorotoxin-Indocyanine Green Conjugate. JAMA Otolaryngol-- Head Neck Surg. 2016; 142:330–8.
23. Tummers QRJG, Hoogstins CES, Gaarenstroom KN, de Kroon CD, van Poelgeest MIE, Vuyk J, et al. Intraoperative imaging of folate receptor alpha positive ovarian and breast cancer using the tumor specific agent EC17. Oncotarget. 2016; 7:32144-32155.
24. Shinden Y, Ueo H, Tobo T, Gamachi A, Utou M, Komatsu H, et al. Rapid diagnosis of lymph node metastasis in breast cancer using a new fluorescent method with γ-glutamyl hydroxymethyl rhodamine green. Sci Rep. 2016; 6:27525.
25. Weissleder R, Tung CH, Mahmood U, Bogdanov A. In vivo imaging of tumors with protease-activated near-infrared fluorescent probes. Nat Biotechnol. 1999; 17:375–8.
26. Mason SD, Joyce JA. Proteolytic networks in cancer. Trends Cell Biol. 2011; 21:228–37.
27. Davies B, Waxman J, Wasan H, Abel P, Williams G, Krausz T, et al. Levels of matrix metalloproteases in bladder cancer correlate with tumor grade and invasion. Cancer Res. 1993; 53:5365–9.
28. Jones JL, Glynn P, Walker RA. Expression of MMP-2 and MMP-9, their inhibitors, and the activator MT1-MMP in primary breast carcinomas. J Pathol. 1999; 189:161–8.
29. Rak B, Garbicz F, Paskal W, Pełka K, Marczewska JM, Wołosz D, et al. The expression of MMP-14 and microRNA-410 in FFPE tissues of human endometrial adenocarcinoma. Histol Histopathol. 2016;11728.
30. Wang Y-Z, Wu K-P, Wu A-B, Yang Z-C, Li J-M, Mo Y-L, et al. MMP-14 overexpression correlates with poor prognosis in non-small cell lung cancer. Tumour Biol J Int Soc Oncodevelopmental Biol Med. 2014; 35:9815–21.
31. Ulasov I, Yi R, Guo D, Sarvaiya P, Cobbs C. The emerging role of MMP14 in brain tumorigenesis and future therapeutics. Biochim Biophys Acta. 2014; 1846:113–20.
32. Zarrabi K, Dufour A, Li J, Kuscu C, Pulkoski-Gross A, Zhi J, et al. Inhibition of matrix metalloproteinase 14 (MMP-14)-mediated cancer cell migration. J Biol Chem. 2011; 286:33167–77.
33. Devy L, Huang L, Naa L, Yanamandra N, Pieters H, Frans N, et al. Selective inhibition of matrix metalloproteinase-14 blocks tumor growth, invasion, and angiogenesis. Cancer Res. 2009; 69:1517–26.
34. Savariar EN, Felsen CN, Nashi N, Jiang T, Ellies LG, Steinbach P, et al. Real-time in vivo molecular detection of primary tumors and metastases with ratiometric activatable cell-penetrating peptides. Cancer Res. 2013; 73:855–64.
35. Hoshida T, Isaka N, Hagendoorn J, Tomaso E di, Chen Y-L, Pytowski B, et al. Imaging Steps of Lymphatic Metastasis Reveals That Vascular Endothelial Growth Factor-C Increases Metastasis by Increasing Delivery of Cancer Cells to Lymph Nodes: Therapeutic Implications. Cancer Res. 2006; 66:8065–75.
36. Schneider CA, Rasband WS, Eliceiri KW. NIH Image to ImageJ: 25 years of image analysis. Nat Methods. 2012; 9:671–5.
37. Barak V, Goike H, Panaretakis KW, Einarsson R. Clinical utility of cytokeratins as tumor markers. Clin Biochem. 2004; 37:529–40.
38. Painter JT, Clayton NP, Herbert RA. Useful immunohistochemical markers of tumor differentiation. Toxicol Pathol. 2010; 38:131–41.
39. Whitney M, Savariar EN, Friedman B, Levin RA, Crisp JL, Glasgow HL, et al. Ratiometric activatable cell-penetrating peptides provide rapid in vivo readout of thrombin activation. Angew Chem Int Ed Engl. 2013; 52:325–30.
40. Kähäri VM, Saarialho-Kere U. Matrix metalloproteinases and their inhibitors in tumour growth and invasion. Ann Med. 1999; 31:34–45.
41. Itoh Y, Nagase H. Matrix metalloproteinases in cancer. Essays Biochem. 2002; 38:21–36.
42. Brown GT, Murray GI. Current mechanistic insights into the roles of matrix metalloproteinases in tumour invasion and metastasis. J Pathol. 2015; 237:273–81.
43. Aguilera TA, Olson ES, Timmers MM, Jiang T, Tsien RY. Systemic in vivo distribution of activatable cell penetrating peptides is superior to that of cell penetrating peptides. Integr Biol Quant Biosci Nano Macro. 2009; 1:371–81.
44. Sharma V, McNeill JH. To scale or not to scale: the principles of dose extrapolation. Br J Pharmacol. 2009; 157:907–21.
45. Leeman MF, Curran S, Murray GI. The structure, regulation, and function of human matrix metalloproteinase-13. Crit Rev Biochem Mol Biol. 2002; 37:149–66.
46. Salaün M, Peng J, Hensley HH, Roder N, Flieder DB, Houlle-Crépin S, et al. MMP-13 In-Vivo Molecular Imaging Reveals Early Expression in Lung Adenocarcinoma. PLoS One. 2015;10:e0132960.

17. (continued) γ-glutamyltranspeptidase-activated fluorescent probe. Sci Transl Med. 2011; 3:110ra119.

47. Yan Q, Yuan Y, Yankui L, Jingjie F, Linfang J, Yong P, et al. The Expression and Significance of CXCR5 and MMP-13 in Colorectal Cancer. Cell Biochem Biophys. 2015; 73:253-259.
48. Rawlings ND, Barrett AJ, Finn R. Twenty years of the MEROPS database of proteolytic enzymes, their substrates and inhibitors. Nucleic Acids Res. 2016;44: D343–50.
49. [Internet] MEROPS - the Peptidase Database. Available from: http://merops.sanger.ac.uk/
50. Julian TB, Blumencranz P, Deck K, Whitworth P, Berry DA, Berry SM, et al. Novel intraoperative molecular test for sentinel lymph node metastases in patients with early-stage breast cancer. J Clin Oncol. 2008; 26:3338–45.
51. Greene FL, Sobin LH. A worldwide approach to the TNM staging system: collaborative efforts of the AJCC and UICC. J Surg Oncol. 2009; 99:269–72.
52. Kircher MF, Weissleder R, Josephson L. A dual fluorochrome probe for imaging proteases. Bioconjug Chem. 2004; 15:242–8.
53. Baeten J, Haller J, Shih H, Ntziachristos V. In vivo investigation of breast cancer progression by use of an internal control. Neoplasia N Y N. 2009; 11:220–7.
54. Tichauer KM, Samkoe KS, Sexton KJ, Gunn JR, Hasan T, Pogue BW. Improved tumor contrast achieved by single time point dual-reporter fluorescence imaging. J Biomed Opt. 2012 17:066001.
55. Hauff SJ, Raju SC, Orosco RK, Gross AM, Diaz-Perez JA, Savariar E, et al. Matrix-Metalloproteinases in Head and Neck Carcinoma–Cancer Genome Atlas Analysis and Fluorescence Imaging in Mice. Otolaryngol--Head Neck Surg Off J Am Acad Otolaryngol-Head Neck Surg. 2014; 151:612–8.
56. Nissinen L, Kähäri V-M. Matrix metalloproteinases in inflammation. Biochim Biophys Acta. 2014; 1840:2571–80.
57. [Internet] Trial of AVB-620 in Women With Primary, Non-Recurrent Breast Cancer Undergoing Surgery. Available from: https://clinicaltrials.gov/ct2/show/NCT02391194